Journal Name

ARTICLE

Phase formations and magnetic properties of single crystal nickel ferrite (NiFe$_2$O$_4$) with different morphology

Aixian Shan,[a,b] Xue Wu,[a] Jing Lu,[b] Chinping Chen[b*] and Rongming Wang[a,c*]

Nickel ferrite (NiFe$_2$O$_4$) nanomaterials with different morphology, including nano-spheres (10-25 nm in diameter), nano-rods (50-60 nm in diameter and ~ 1 μm in length), and nano-octahedrons (side length ~ 150 nm), had been synthesized by a single mild hydrothermal method at 160 ℃ without any surfactant. Crystal structures have been investigated by TEM, HRTEM, and studied by simulations of Material Studio program. The variations in the morphology, as well as the preferential crystal growth directions, depend only on the pH value of the reaction solutions. A phase formation mechanism is thus proposed. Magnetization measurements at T = 300 K indicate that the NiFe$_2$O$_4$ nano-spheres with 10-25 nm in diameter are superparamagnetic with non-saturating magnetization at H = 7 kOe. The saturation magnetization, M_S, of the nanorods is 40 emu/g, less than the bulk value, M_S = 46.7 to 55 emu/g. The coercivity is H_C = 40 Oe, reduced from the bulk value of 100 Oe. On the other hand, the nano-octahedrons have a saturation magnetization of M_S = 50 emu/g, the same as the bulk. However the coercively, H_C = 50 Oe is also much reduced from the bulk.

Keywords: Nickel ferrite nanoparticle, phase formation, morphology control, magnetic properties

Introduction

Nickel ferrite (NiFe$_2$O$_4$) have received a lot of attentions recently, due to various applications in spintronics[1], microwave absorption[2], catalyst[3], gas sensors[4], hydrogen production[5], lithium ion batteries[6], even in biomedicine[7] etc. As more and more attentions have been devoted to the nano-sized magnetic materials for their unique properties compared to their bulk counterparts, the scientific interest on nano-sized NiFe$_2$O$_4$ is on the rising.

The magnetism of NiFe$_2$O$_4$ is particularly interesting due to its significant saturation magnetization and unique magnetic structures. NiFe$_2$O$_4$ has an inverse spinel structure with Ni^{2+} ions on octahedral B sites (denoted as O_h-sites) and Fe^{3+} ions on both of the tetrahedral A (denoted as T_d-site) and the O_h-sites equally. This is supported by the calculation of formation energy in favor of the reverse spinel rather than the spinel structure.[8] However, the NiFe$_2$O$_4$ nanoparticles are found to have the mixed spinel structure with the inverse one,[9-11] i.e., some Ni^{2+} ions may occupy the T_d sites. A general formula for a nickel ferrite structure is (Ni$_{1-x}$Fe$_x$)[Ni$_x$Fe$_{2-x}$]O$_4$, where x is the degree of inversion. According to the crystal field theory, the magnetic moments are arising from the local moments of the Ni^{2+} with $3d^8$ electrons and Fe^{3+} with $3d^5$ electrons. The net magnetization comes from the Ni^{2+} (O_h) cations alone, ~ 2 μ_B,

whereas the Fe^{3+} moments ~ 5μ_B in a high spin state for both the O_h and T_d sites are antiparallel and cancel with each other. This leads to an overall moment of 2 μ_B/formula unit (FU),[12] equal to the saturation magnetization, M_S = 50 emu/g. In addition, calculations by density functional theory (DFT) yield a consistent result for the magnetic moment of the inverse spinel NiFe$_2$O$_4$, ~ 2μ_B/FU.[8]

Various methods have been developed to synthesize NiFe$_2$O$_4$ nanoparticles, such as co-precipitation[13], sol-gel[14], spray pyrolysis[15], mechanical activation[16] and hydrothermal method[17-19]. Among these methods, hydrothermal method has been extensively used due to better controllability of morphology and size.

In this paper, the morphological control of NiFe$_2$O$_4$ nanoparticles with different particle size has been carried out by using a facile hydrothermal method at a relatively mild temperature of 160 ℃. Only three chemicals are used without the application of any surface modifier. The phase formation mechanism and the magnetic properties are studied.

Experimental details

The NiFe$_2$O$_4$ nanomaterials with different morphology have been synthesized by a hydrothermal method. In a typical process, aqueous solutions of Ni(NO$_3$)$_2$•6H$_2$O (0.05 M 20 mL)

and $Fe(NO_3)_2 \cdot 9H_2O$ (0.1 M 20 mL) were mixed thoroughly. Under magnetic stirring, a certain volume of NaOH aqueous solutions (3 M) was then added into the mixed solution dropwise. The pH value of the solution was measured and recorded. Then, the obtained brown colloidal suspension was kept stirring for 1 hour. Afterwards, the solution was moved into an autoclave, which was kept at 160 ℃ for 10 h. Dark brown precipitations of $NiFe_2O_4$ were yielded. A power collection of $NiFe_2O_4$ was obtained after a centrifugation, then washed three times with ethyl alcohol and deionized water and dried in vacuum drying oven. The final product was reddish brown. All of the chemicals above-mentioned were analytical grade and used as received. The samples with different components and morphologies were obtained by adjusting the pH of the reaction system.

The morphologies and chemical compositions of the as-synthesized products were characterized by using X-ray diffraction (XRD, X' Pert Pro MPD system, Cu Ka, λ = 0.154 nm), scanning electron microscopy (SEM, Hitachi S-4800), and transmission electron microscopy (TEM, JEOL 2100F at 200 kV) equipped with an energy dispersive X-ray spectroscope (EDS). TEM samples were prepared by dispersing the powder in ethanol with ultrasonic treatment and then dropping such solution on a Cu-grid coated with porous carbon film. The magnetic properties of the as-synthesized powder samples were measured using a vibrating sample magnetometer (VSM, LakeShore 7400). The $M(H)$ curves were measured at room temperature (RT) with the applied field swept from -7 kOe to 7 kOe.

Results and discussion

(1) Characterization
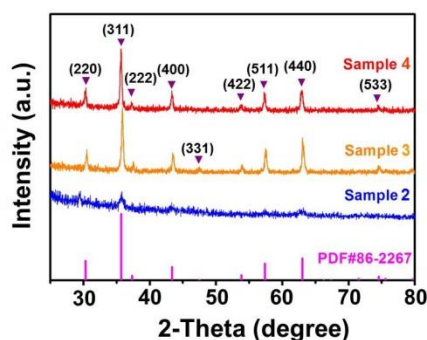
Fig. 1 XRD patterns of samples 2, 3 and 4 indexed to $NiFe_2O_4$ (JCPDF No. 86-2267).

The samples labelled as 1, 2, 3 and 4 are obtained by adjusting the pH value of reaction solutions to 5, 7, 12 and 13 respectively. In particular, sample 1 is rhombohedral a-Fe_2O_3. Detailed characterizations and properties for applications with sample 1 will be presented elsewhere. The present paper will rather focus on the investigations of nickel ferrites, which are samples 2, 3 and 4. The EDS results show that these three samples contain only three elements, i.e., nickel, iron and oxygen. The XRD patterns of these three samples, as shown in

Fig.1, fit with the reference patterns of cubic structure $NiFe_2O_4$ (JCPDS no. 86-2267). No extra reflections from impurities are detected, suggesting the high purity of the as-synthesized products.
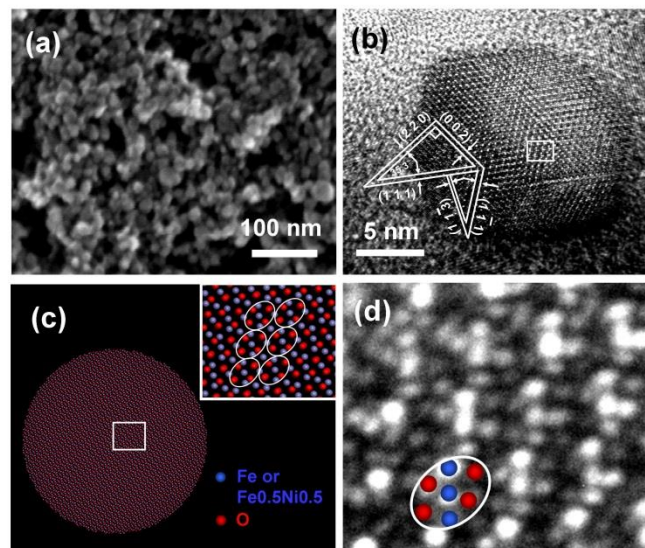
Fig. 2 Microstructures of the as-prepared sample 2: (a) An overview SEM image revealing a spherical morphology about 10-25 nm in diameter; (b) HRTEM image of a single nano-sphere projected from <1 -1 0>; (c) schematic illustration by Material Studio for $NiFe_2O_4$ nano-sphere projected along the [1 -1 0] axis. The red solid dot is for O atom. The blue one is for Fe atom or $Ni_{0.5}Fe_{0.5}$. The inset is a close-up version for the white square area; (d) the enlarged phase image for the white square area in image (b). The circles in the inset of figure (c) and in figure (d) show the same structure unit and atomic column for the corresponding positions.

Fig. 2(a), a low magnification SEM image of sample 2, shows typical spherical morphologies. $NiFe_2O_4$ nano-spheres with a size of 10-25 nm were yielded with the pH value adjusted to 7. These $NiFe_2O_4$ nano-spheres congregated together presumably due to their high surface energy and magnetic dipolar interaction. Fig. 2 (b), the HRTEM image for a single nano-sphere, shows a single crystal structure. The <1 -1 0> zone axis, along which the figure was taken, is determined by the lattice spacing and the relative angles of the axis of the crystal growth planes, on top of the XRD information shown in Fig. 1 (c). The atoms stacking model for the $NiFe_2O_4$ nano-spheres is then constructed by Materials Studio (MS) software[20, 21]. The atomic structure of the ferrite is provided by NIMS Materials Database (MatNavi) as an input to the MS software. Fig. 2 (c) is the graph of atoms stacking model for the $NiFe_2O_4$ nano-sphere projected along the [1 -1 0] axis. To show more clearly, the white square area in Figs. 2 (b) and (c) are enlarged, put in Fig. 2 (d) and the inset of Fig. 2 (c) respectively. By these two enlarged figures, one finds the same unit of atoms enclosed by the white circles. It further supports this 3D atoms stacking model. From the 3D model, we can find the atoms are the same in each atom column. It is noted that iron or nickel atoms are indistinguishable in this structure, and hence treated equally in the model. They have, however, different contrast from the oxygen under HRTEM as shown in Fig. 2(d).
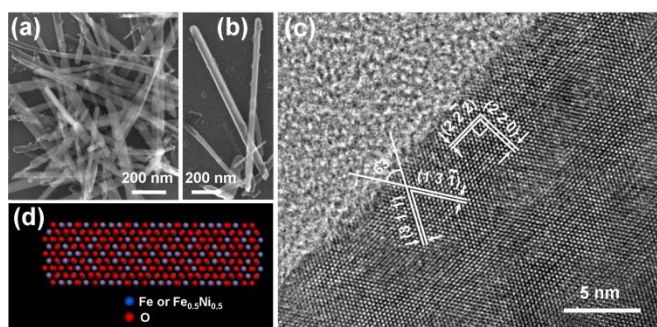
Fig. 3 Microstructures of the as-prepared sample 3: (a) an overview by an SEM image revealing a rod-like morphology. (b) an SEM image for two nano-rods with the length of ~ 1 μm and diameter of ~ 50-60 nm (c) HRTEM image of part of a $NiFe_2O_4$ nano-rod projected from <-1 1 2>; (d) atoms stacking model of $NiFe_2O_4$ nano-rod projected along the [-1 1 2] axis.

Sample 3, the nickel ferrite nano-rods, was yielded at the pH value of 12. Nano-rod morphology in a low magnification SEM image is shown in Fig. 3 (a). Typical length of about 1 μm and diameter of about 50-60 nm is revealed by another SEM image in Fig. 3 (b). The HRTEM image, Fig.3 (c), of a typical $NiFe_2O_4$ nano-rods taken from <-1 1 2> zone axis shows a single crystal structure. The growth direction of the $NiFe_2O_4$ nano-rods is determined to be [1 1 0]. The atoms stacking model for the $NiFe_2O_4$ nano-rod is constructed along [1 1 0] by the commercial software MS. However, Fig. 3 (d) is $NiFe_2O_4$ nano-rod projected along the [-1 1 2] axis. The atomic arrangement in Fig. 3 (d) is the same as that observed experimentally shown in Fig. 3 (c).
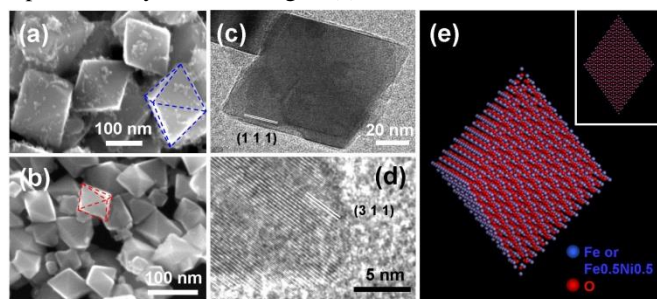
Fig. 4 Microstructures of the as-prepared sample 4: (a) An overview SEM image revealing a octahedral morphology. The length of each side is ~ 150 nm. There are some even much smaller nanoparticles appear on the surface of $NiFe_2O_4$ nano-octahedrons. (b) An overview SEM image showing $NiFe_2O_4$ nano-octahedron with clean surface. The length of each side is ~ 60 nm. (c) and (d) are HRTEM images of $NiFe_2O_4$ nano-octahedron projected from <0 1 -1> showing a single-crystal structure; (e) Atoms stacking model of $NiFe_2O_4$ nano-octahedron. The inset shows the graph of the atoms stacking model projected along the [0 1 -1] axis.

The SEM image in Fig. 4 shows the general octahedral morphology of sample 4 obtained by the pH value of 13. The facets of the octahedrons are distinguishable and the edge for one of the octahedral $NiFe_2O_4$ particles is drawn in Fig. 4 (a) using the blue dotted line. The length of each side is about 150 nm. Clearly, there are some barely visible nanoparticles on the surface of the $NiFe_2O_4$ nano-octahedrons. By adding 50 mg cetyltrimethyl ammonium bromide (CTAB) to the reaction solution, the $NiFe_2O_4$ nano-octahedrons are obtained with clean surfaces, as shown in Fig. 4 (b). Furthermore, the length of each side is reduced to ~ 60 nm. Further observations on the facet

structure of the octahedrons are conducted by TEM and HRTEM. Figs. 4 (c) and (d) show the morphologies of octahedrons viewed along the <0 1 -1> projection directions. The consistent lattice orientation of the octahedral particles reveals the single crystalline nature shown in Fig. 4 (c). The variations in brightness from the center of the images to the left and the right sides of the nano-octahedron reflect the corresponding variations of sample thickness, which could be ascribed to the octahedral shape of the nano-crystals. As shown in Figs. 4(c) and (d), the faces (1 1 1) and (3 1 1) can be observed, respectively. In addition, the planes exposed are determined for it is in parallel with the sides of the nano-crystals. Fig. 4(e) is from the atoms stacking model for $NiFe_2O_4$ nano-octahedron. The inset is for the projection graph along the [0 1 -1] axis, along which direction the HRTEM images were taken.

(2) Crystal growth mechanism
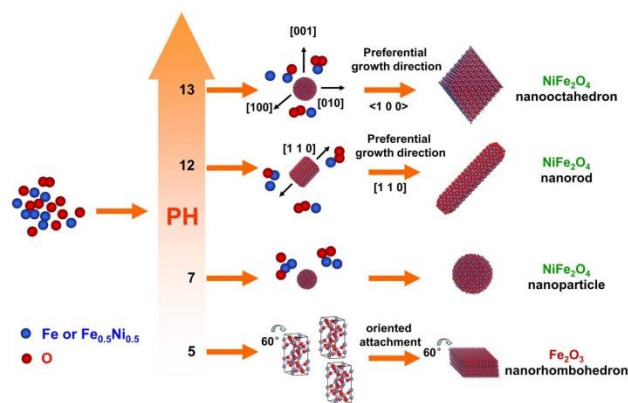
Fig.5 Schematic illustration for the formation processes of α-Fe_2O_3 nano-rhombohedrons and $NiFe_2O_4$ nanoparticles with various morphologies obtained by adjusting the pH value for the reaction solution.

The solubility products (Ksp) for $Fe(OH)_3$ and $Ni(OH)_2$ are 2.79×10^{-39} and 2×10^{-15}, respectively. Correspondingly, the pH values at equilibrium are 1.5 and 6.7 respectively when $Fe(OH)_3$ and $Ni(OH)_2$ begin to precipitate. In the reaction, NaOH provides OH^- to precipitate or to reduce the concentration of the two metal ions, i.e. Fe^{3+} and Ni^{2+}. At pH equal to 5, Ni^{2+} with higher solubility remains in the solution without participating into the reaction. $Fe(OH)_3$ transforms to FeOOH under the conditions of high temperature and high pressure. Over time, FeOOH further transforms to α-Fe_2O_3.[22, 23] With the pH equal to or greater than 7, $Ni(OH)_2$ precipitation occurs in the solution. The precipitated $Ni(OH)_2$ would react with FeOOH to form $NiFe_2O_4$ under hydrothermal condition.[24, 25] The reactions could be described as follows:

$$Fe^{3+} + 3OH^- \rightarrow Fe(OH)_3 \qquad (1)$$
$$Fe(OH)_3 \rightarrow FeOOH + H_2O \qquad (2)$$
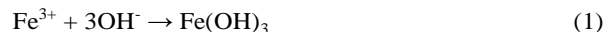
(a) When pH was under 6.7:
$$2FeOOH \rightarrow \alpha\text{-}Fe_2O_3 + H_2O \qquad (3)$$

(b) When pH is was above 6.7:
$$Ni^{2+} + 2OH^- \rightarrow Ni(OH)_2 \qquad (4)$$
$$Fe(OH)_3 \rightarrow FeOOH + H_2O \qquad (5)$$

$$2FeOOH + Ni(OH)_2 \rightarrow NiFe_2O_4\downarrow + 2H_2O \qquad (6)$$
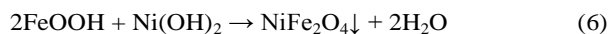
In general, pH value is an indicator reflecting the concentration of Fe^{3+} and Ni^{2+} ions in the solution. Obviously, the kinematics of the crystal growth along different crystal directions determines the morphology of the products. Hence the growth rate of different crystallographic facets depends on both of the ionic concentrations. For high concentration of Fe^{3+} ions without the presence of nickel ions, with the pH value equal to 5 or even smaller, the {1 0 4} surfaces are the lowest energy during crystalization, resulting in the formation of α-Fe_2O_3 rhombohedrons[26] Besides, the primitive cell of α-Fe_2O_3 is rhombohedral-center hexagonal structure. It leads to the most stable configuration for the α-Fe_2O_3 nanoparticles with the rhombohedral morphology showing six {1 0 4} surfaces through the hydrolysis of ferric chloride even at room temperature.[27, 28]

With the pH value equal to or greater than 7, concentration of Ni^{+2} ions increases sharply in the solution, favoring the formation of nickel ferrites. The preferential growth direction during crystallization depends on the concentration of Ni^{2+} ions, hence different morphology of the $NiFe_2O_4$ nanomaterials. Without surfactant, the pH value is a crucial factor to tailor the morphologies by controlling the reaction kinetics.[29, 30]

With the pH value adjusted to 7, the crystalline growth rates from every direction are almost equal, hence, preferring the spherical morphology for the $NiFe_2O_4$ nanoparticles. However, at the pH value of 12, the growth rate along [1 1 0] direction is the fastest, leading to the rod-like $NiFe_2O_4$. With the pH value increasing to 13, the crystal growth favors along <1 0 0> rather than along <1 1 1>. So, the {1 1 1} facets are exposed, which results in the formation of the $NiFe_2O_4$ nano-octahedrons.

(3) Magnetic property

The magnetic hysteresis loops of the $NiFe_2O_4$ samples were measured by VSM at 300 K in the range of -7 to 7 kOe, as shown in Fig. 6. The saturation magnetization for the nano-octahedrons with a side length of about 150 nm is about 55 emu/g, approximately equal to 2.3 μ_B/FU (formula unit). This value is calculated as 50 emu/g using Neel's sub lattice theory for cubic inverse spinel $NiFe_2O_4$.[31] This is reasonably consistent with the calculated value 2.0 μ_B/FU by DFT[8] and the reported experimental values ranging from 46.7 to 55.0 emu/g.[25, 32-34] The nano-rods, smaller in the characteristic dimension, ~ 50 nm in diameter, have a lower M_S value, M_S ~ 40 emu/g. For the spherical nanoparticles which have even much smaller size, 15 ~ 25 nm in diameter, the magnetization does not show a sign reaching saturation in the field of 7 KOe. Obviously, the nanoparticles with increasing surface-to-volume ratio have decreasing saturation magnetization. This behavior might be attributed to the spin-canting anomaly, with which the fine ferromagnetic iron-oxide particles are not completely saturated by large magnetic fields,[35] or due to a spin-glass-like surface layer.[32] On the other hand, the bulk saturation magnetization is uncertain within 10% to the value of 50 emu/g reported in the literatures mentioned above. This might be due

to the compositional variation from the stoichiometric ratio, such as $Ni_{(1+x)}Fe_{(2-x)}O_4$ with - 0.1 < x < 0.1, assuming Ni ions possessing roughly the same magnetic moment. Perhaps, in our case with the nickel ferrite nanoparticles, although the EDS measurements lead to the elemental ratio of Fe over Ni close to 2 and the XRD results give the $NiFe_2O_4$ crystal structure, still, it casts reasonable doubts that nonstoichiometric variation might be responsible partially for the observed difference in the saturation magnetization.
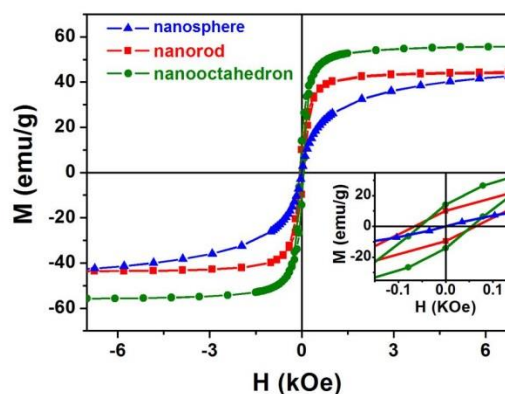
Fig.6 Magnetization cures of the $NiFe_2O_4$ samples versus the applied field at 300 K. The inset is the enlargements in the low field.

The coercivities of the $NiFe_2O_4$ samples with morphologies of nano-octahedrons and nano-rods are very close to each other, H_C ~ 50 Oe. However, for the $NiFe_2O_4$ nanospheres, the coercivity goes to zero, showing the superparamagnetic behaviors. Apparently, the shape anisotropy and the particle size are crucial to the magnetization reversal properties. Spherical $NiFe_2O_4$ nanoparticles with the size of 10 ~ 25 nm, might be in the superparamagnetic regime. It is noteworthy that in comparison to the bulk counterpart, the $NiFe_2O_4$ octahedral and rod-like samples exhibit a reduced coercivity, i.e., H_C ~ 100 Oe for the bulk versus 50 Oe for the present nano-samples. Consensus is yet to be reached in this respect. Some have reported a reduced coercivity for the nano-sized nickel ferrite, whereas some others have shown otherwise.[33] Significant reduction in the coercivity might also arise from the magnetic dipolar interaction with the powder sample to reduce the magnetostatic energy.[36]

Specifically, for the $NiFe_2O_4$ nano-octahedrons, the saturation magnetization is close to that of the bulk, however, with only a half of the coercivity. This gives an application potential as a soft magnetic material.

Conclusions

$NiFe_2O_4$ nano-spheres, nano-rods, nano-octahedrons had been synthesized by a facile hydrothermal method without any surfactant. The pH value is a crucial factor to the morphologies, the crystal growth directions and even the compositions of the products. These nanomaterials are single crystal with definite growing direction as investigated by TEM, HRTEM, and

studied by the crystal structure simulation. Magnetic measurements indicate that the $NiFe_2O_4$ nano-sphere with 10 - 25 nm in diameter is superparamagnetic with a non-saturating magnetization at the field under 7 kOe. Whereas, the large nano-octahedral sample, about 150 nm in side length, exhibits the bulk saturation magnetization, ~ 55 emu/g at 300 K, with a reduced coercivity, ~ 50 Oe from the bulk value of 100 Oe.

Acknowledgements

Notes and references

a Department of Physics, Beihang University, Beijing 100191, China;

b Department of Physics, Peking University, Beijing 100871, China;

c School of Mathematics and Physics, University of Science and Technology Beijing, Beijing 100083, China;

* To whom correspondence should be addressed.

E-mail: cpchen@pku.edu.cn; rmwang@buaa.edu.cn

1. U. Luders, A. Barthelemy, M. Bibes, K. Bouzehouane, S. Fusil, E. Jacquet, J. P. Contour, J. F. Bobo, J. Fontcuberta and A. Fert, *Adv Mater*, 2006, **18**, 1733-1736.
2. X. Gu, W. M. Zhu, C. J. Jia, R. Zhao, W. Schmidt and Y. Q. Wang, *Chem Commun*, 2011, **47**, 5337-5339.
3. R. Benrabaa, A. Lofberg, A. Rubbens, E. Bordes-Richard, R. N. Vannier and A. Barama, *Catal Today*, 2013, **203**, 188-195.
4. A. Sutka, *Sensor Lett*, 2013, **11**, 2010-2013.
5. R. Fernandez-Saavedra, M. B. Gomez-Mancebo, C. Caravaca, M. Sanchez, A. J. Quejido and A. Vidal, *Int J Hydrogen Energ*, 2014, **39**, 6819-6826.
6. Y. S. Fu, Y. H. Wan, H. Xia and X. Wang, *J Power Sources*, 2012, **213**, 338-342.
7. H. Yin, H. P. Too and G. M. Chow, *Biomaterials*, 2005, **26**, 5818-5826.
8. H. Perron, T. Mellier, C. Domain, J. Roques, E. Simoni, R. Drot and H. Catalette, *J Phys-Condens Mat*, 2007, **19**, 346219.
9. C. N. Chinnasamy, A. Narayanasamy, N. Ponpandian, K. Chattopadhyay, K. Shinoda, B. Jeyadevan, K. Tohji, K. Nakatsuka, T. Furubayashi and I. Nakatani, *Phys Rev B*, 2001, **63**, 184108.
10. A. B. Nawale, N. S. Kanhe, K. R. Patil, S. V. Bhoraskar, V. L. Mathe and A. K. Das, *J Alloy Compd*, 2011, **509**, 4404-4413.
11. C. Agrafiotis, A. Zygogianni, C. Pagkoura, M. Kostoglou and A. G. Konstandopoulos, *Aiche J*, 2013, **59**, 1213-1225.
12. G. H. Jaffari, A. K. Rumaiz, J. C. Woicik and S. I. Shah, *J Appl Phys*, 2012, **111**, 093906.
13. P. Sivakumar, R. Ramesh, A. Ramanand, S. Ponnusamy and C. Muthamizhchelvan, *Mater Lett*, 2011, **65**, 483-485.
14. P. Lavela and J. L. Tirado, *J Power Sources*, 2007, **172**, 379-387.
15. D. S. Jung and Y. C. Kang, *J Magn Magn Mater*, 2009, **321**, 619-623.
16. Z. H. Zhou, J. M. Xue, J. Wang, H. S. O. Chan, T. Yu and Z. X. Shen, *J Appl Phys*, 2002, **91**, 6015-6020.
17. J. Zhou, J. F. Ma, C. Sun, L. J. Xie, Z. Q. Zhao, H. Tian, Y. G. Wang, J. T. Tao and X. Y. Zhu, *J Am Ceram Soc*, 2005, **88**, 3535-3537.
18. M. Fu, Q. Z. Jiao and Y. Zhao, *J Mater Chem A*, 2013, **1**, 5577-5586.
19. H. Zhao, Y. M. Dong, G. L. Wang, P. P. Jiang, J. J. Zhang, L. N. Wu and K. Li, *Chem Eng J*, 2013, **219**, 295-302.
20. B. Delley, *J Chem Phys*, 1990, **92**, 508-517.
21. B. Delley, *J Chem Phys*, 2000, **113**, 7756-7764.
22. M. Lin, L. Tng, T. Y. Lim, M. Choo, J. Zhang, H. R. Tan and S. Q. Bai, *J Phys Chem C*, 2014, **118**, 10903-10910.
23. S. K. Kwon, K. Kimijima, K. Kanie, A. Muramatsu, S. Suzuki, E. Matsubara and Y. Waseda, *Isij Int*, 2005, **45**, 77-81.
24. M. Menelaou, K. Georgoula, K. Simeonidis and C. Dendrinou-Samara, *Dalton T*, 2014, **43**, 3626-3636.
25. H. Li, H. Z. Wu and G. X. Xiao, *Powder Technol*, 2010, **198**, 157-166.
26. Z. Liu, B. L. Lv, D. Wu, Y. H. Sun and Y. Xu, *Particuology*, 2013, **11**, 327-333.
27. M. Lin, H. R. Tan, J. P. Y. Tan and S. Q. Bai, *J Phys Chem C*, 2013, **117**, 11242-11250.
28. R. D. Rodriguez, D. Demaille, E. Lacaze, J. Jupille, C. Chaneac and J. P. Jolivet, *J Phys Chem C*, 2007, **111**, 16866-16870.
29. C. J. DeSantis, A. C. Sue, M. M. Bower and S. E. Skrabalak, *Acs Nano*, 2012, **6**, 2617-2628.
30. J. A. Zhang, M. R. Langille and C. A. Mirkin, *J Am Chem Soc*, 2010, **132**, 12502-12510.
31. M. George, A. M. John, S. S. Nair, P. A. Joy and M. R. Anantharaman, *J Magn Magn Mater*, 2006, **302**, 190-195.
32. R. H. Kodama, A. E. Berkowitz, J. E. J. McNiff and S. Foner, *Phys Rev Lett*, 1996, **77**, 394-397.
33. V. Sepelak, I. Bergmann, A. Feldhoff, P. Heitjans, F. Krumeich, D. Menzel, F. J. Litterst, S. J. Campbell and K. D. Becker, *J Phys Chem C*, 2007, **111**, 5026-5033.
34. K. K. Bharathi, K. Balamurugan, P. N. Santhosh, M. Pattabiraman and G. Markandeyulu, *Phys Rev B*, 2008, **77**, 172401.
35. A. Hajalilou, M. Hashim, R. Ebrahimi-Kahrizsangi, H. M. Kamari and N. Sarami, *Ceram Int*, 2014, **40**, 5881-5887.
36. W. M. Chen, C. P. Chen and L. Guo, *J Appl Phys*, 2010, **108**, 043912.
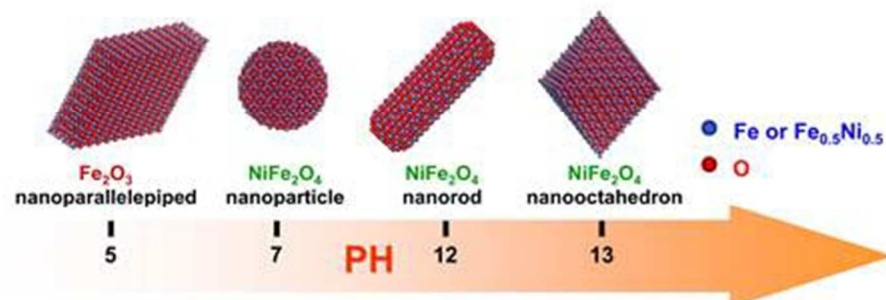
Nickel ferrite nanomaterials with different morphology, including nano-spheres, nano-rods and nano-octahedrons had been synthesized by a single mild hydrothermal method at 160 °C without any surfactant.
79x39mm (150 x 150 DPI)